nature communications

Article

https://doi.org/10.1038/s41467-024-52083-1

Secondary metal ion-induced electrochemical reduction of U(VI) to U(IV) solids

Received: 2 April 2024

Accepted: 26 August 2024

Published online: 04 September 2024

Check for updates

Xiaolu Liu[1,2], Yinghui Xie[1], Mengjie Hao[1], Yang Li[1], Zhongshan Chen[1], Hui Yang[1] ✉, Geoffrey I. N. Waterhouse[3], Xiangke Wang[1] ✉ & Shengqian Ma[2] ✉

Recent studies have shown that aqueous U(VI) ions can be transformed into U(VI) precipitates through electrocatalytic redox reactions for uranium recovery. However, there have been no reports of U(IV) solids, such as UO_2, using electrochemical methods under ambient conditions since low-valence states of uranium are typically oxidized to U(VI) by O_2 or H_2O_2. Here we developed a secondary metal ion-induced strategy for electrocatalytic production of U(IV) solids from U(VI) solutions using a catalyst consisting of atomically dispersed gallium on hollow nitrogen-doped carbon capsules ($Ga-N_x-C$). This method relies on the presence of secondary metal ions, e.g., alkaline earth metals, transition metals, lanthanide metals, and actinide metals, which promote the generation of UO_2 or bimetallic U(IV)-containing oxides through a two-electron transfer process. No U(IV) solid products were generated in the presence of alkali metal ions. Mechanistic studies revealed that the strong binding affinity between U(IV) and alkaline earth metals (Ca^{2+}/Mg^{2+}/Sr^{2+}/Ba^{2+}), transition metals (Ni^{2+}/Zn^{2+}/Pb^{2+}/Fe^{3+}, etc.) and lanthanide/actinide metals (Ce^{4+}/Eu^{3+}/Th^{4+}/La^{3+}) suppressed re-oxidation of U(IV) to U(VI), leading to the generation of $U(IV)O_2$ and M_x(M = Ce, Eu, Th, La)$U(IV)_yO_2$. This work provides fundamental insights into the electrochemical behavior of uranium in aqueous media, whilst guiding uranyl capture from nuclear waste and contaminated water.

Nuclear energy is expected to play an important role in achieving net-zero carbon emissions across the energy sector[1–3]. ^{235}U is the most important fission fuel used in nuclear reactors, with this fuel being produced by enrichment of mined uranium ore[4,5]. However, waste and tailings from uranium mining can result in the release of uranium into the environment, leading to contaminated groundwater and hazards to the environment and human health (30 ppb stated by Environmental Protection Agency)[6–10]. Furthermore, the plutonium uranium reduction extraction (PUREX) process used to purify uranium creates significant uranium-containing waste (~several hundred ppm levels)[11,12]. The limited amounts of uranium ore on land motivate the search for methods of extracting uranium from seawater (it is estimated that there is ~1000 times the amount of uranium in the Earth's oceans than on land)[13–16]. Accordingly, researchers are now seeking efficient technologies and methods for extracting or removing uranium from mining waste, nuclear waste, seawater, and contaminated water, thus addressing both uranium resource recovery/utilization and environmental remediation[17,18].

[1]College of Environmental Science and Engineering, North China Electric Power University, 102206 Beijing, PR China. [2]Department of Chemistry, University of North Texas, Denton, TX 76201, USA. [3]School of Chemical Sciences, The University of Auckland, Auckland 1142, New Zealand.
✉e-mail: h.yang@ncepu.edu.cn; xkwang@ncepu.edu.cn; shengqian.ma@unt.edu

In aqueous media, uranium typically exists in the form of hexavalent uranyl ions [$U(VI)O_2^{2+}$]. Reduction of soluble U(VI) into tetravalent U(IV) solids (such as UO_2) is considered a promising way to extract and remove uranium from waste solutions and contaminated water[19,20]. Traditionally, chemical reduction methods have been used for this purpose, though require chemical reagents that generate a large amount of secondary waste[21–23]. Adsorption is the most widely used technology for uranium extraction from seawater, but it is limited by slow adsorption kinetics and finite number of adsorption sites[24]. Electrochemical deposition methods, which use electricity rather than chemicals, represent a promising alternative way to extract uranium under various conditions. A half-wave rectified alternating current electrochemical method was reported for uranium extraction from seawater, yielding a U(VI) solid $(UO_2)O_2{\cdot}xH_2O$ product through electron transfer and achieving a high capacity under wide-ranging conditions of pH and ionic strength[25]. U(VI) can also be reduced to stabilized U(V) on the surface of magnetite via a one-electron transfer by controlling the applied voltage[26]. Subsequently, an adsorption-electrocatalytic method was developed for uranium extraction, wherein atomically dispersed Fe-N_x or In-N_x sites served as a reversible electron transfer platform that transformed adsorbed U(VI) to solid $Na_2O(UO_3{\cdot}H_2O)_x$ precipitates in the presence of sodium ions (through stepwise one-electron reduction/oxidation processes) found in seawater[27–29]. Furthermore, a reusable functional graphene-foam electrode was developed for uranium extraction under various conditions, which yielded a quasi-2D $U(VI)O_2(OH)_2$ layered product. These works demonstrate the potential of electrochemical approaches for uranium extraction and removal from aqueous media[30]. However, to date, there have been no reports of U(VI) being reduced to U(IV) solid products by electrochemical methods under ambient conditions (Fig. 1a and Supplementary Table 1). If discovered, such methods might facilitate uranium extraction and removal from seawater, mining waste, nuclear waste, and contaminated water, motivating the current work.

Herein, we report a general secondary metal ion-induced strategy for electrocatalytic reducing aqueous uranyl ions to UO_2 or bimetallic M_x(M = Ce, Eu, Th, La)U_yO_2 solid products. In the presence of certain secondary metal ions, Ga-N_x-C electrocatalyst could generate U(IV) solid products under various conditions (Fig. 1b). In the presence of alkaline earth metals or transition metals, solid UO_2 was obtained under square-wave voltammetry conditions (Fig. 1c). In the presence of lanthanide or actinide metal ions, a family of M_x(M = Ce, Eu, Th, La)U_yO_2 oxides were obtained (Fig. 1c). The generated $M_xU_yO_2$ were insoluble under acidic solutions, demonstrating excellent chemical stability. This straightforward method prevents the undesirable re-oxidation of U(IV) back to U(VI). This developed technique is expected to be applicable for uranium extraction from nuclear waste, contaminated water, and seawater.

Results

Hollow Ga-N_x-C capsule synthesis and characterization

The synthesis of the hollow Ga-N_x-C capsules is shown in Fig. 2a. In brief, ZIF-8 and ZIF-8@K-TA nanocrystals were synthesized following a previously reported process with slight modification[31,32]. Then, ZIF-8@K-TA was added into a methanol solution containing gallium ions to exchange the potassium ions, yielding ZIF-8@Ga-TA which retained

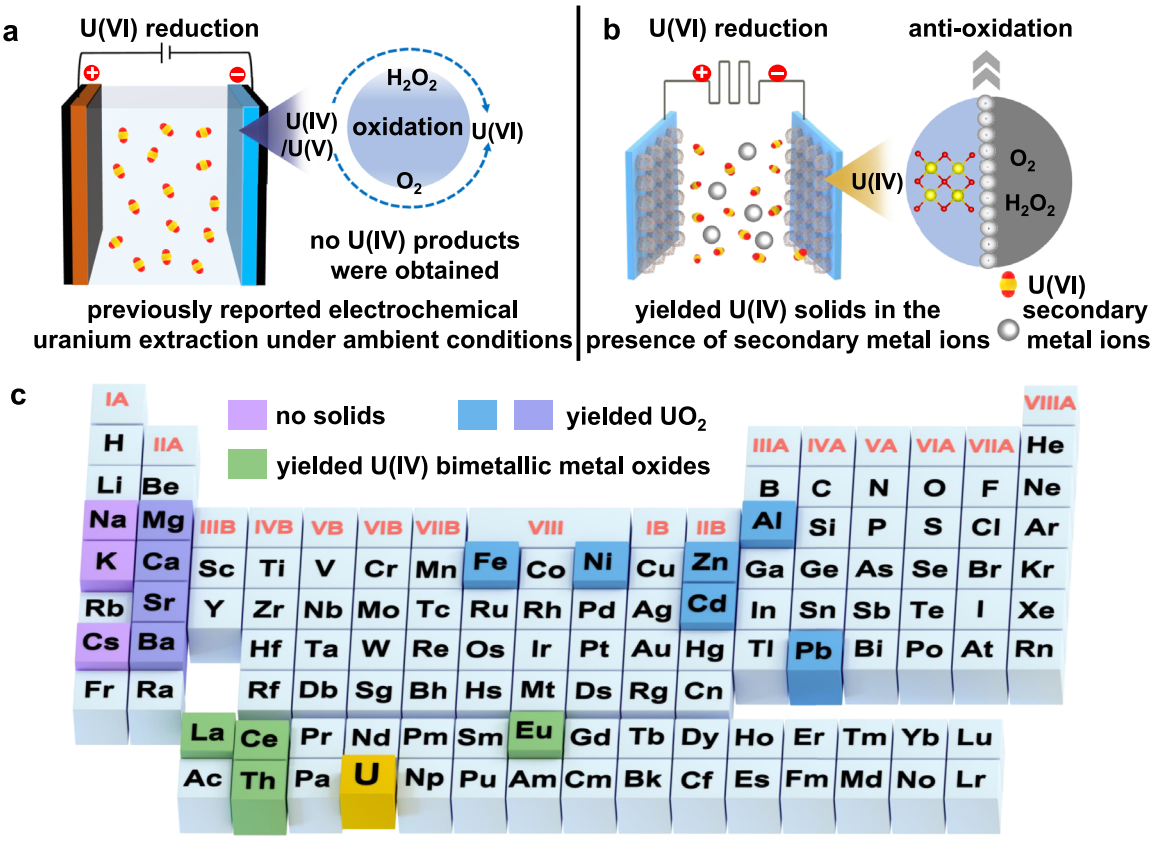

Fig. 1 | The general strategy for secondary metal ion-induced electrochemical U(VI) reduction to U(IV) solid products developed in our study. a Schematic illustration of previously reported electrochemical approaches for uranium extraction from aqueous solution under ambient conditions (no U(IV) products were obtained). **b** Schematic illustration of our strategy for the generation of U(IV) products in the presence of various secondary metal ions (products formed include UO_2 and U(IV) bimetallic metal oxides). **c** Summary of the secondary metals evaluated in this work for the electrocatalytic transformation of aqueous U(VI) to U(IV) solid products.

https://doi.org/10.1038/s41467-024-52083-1

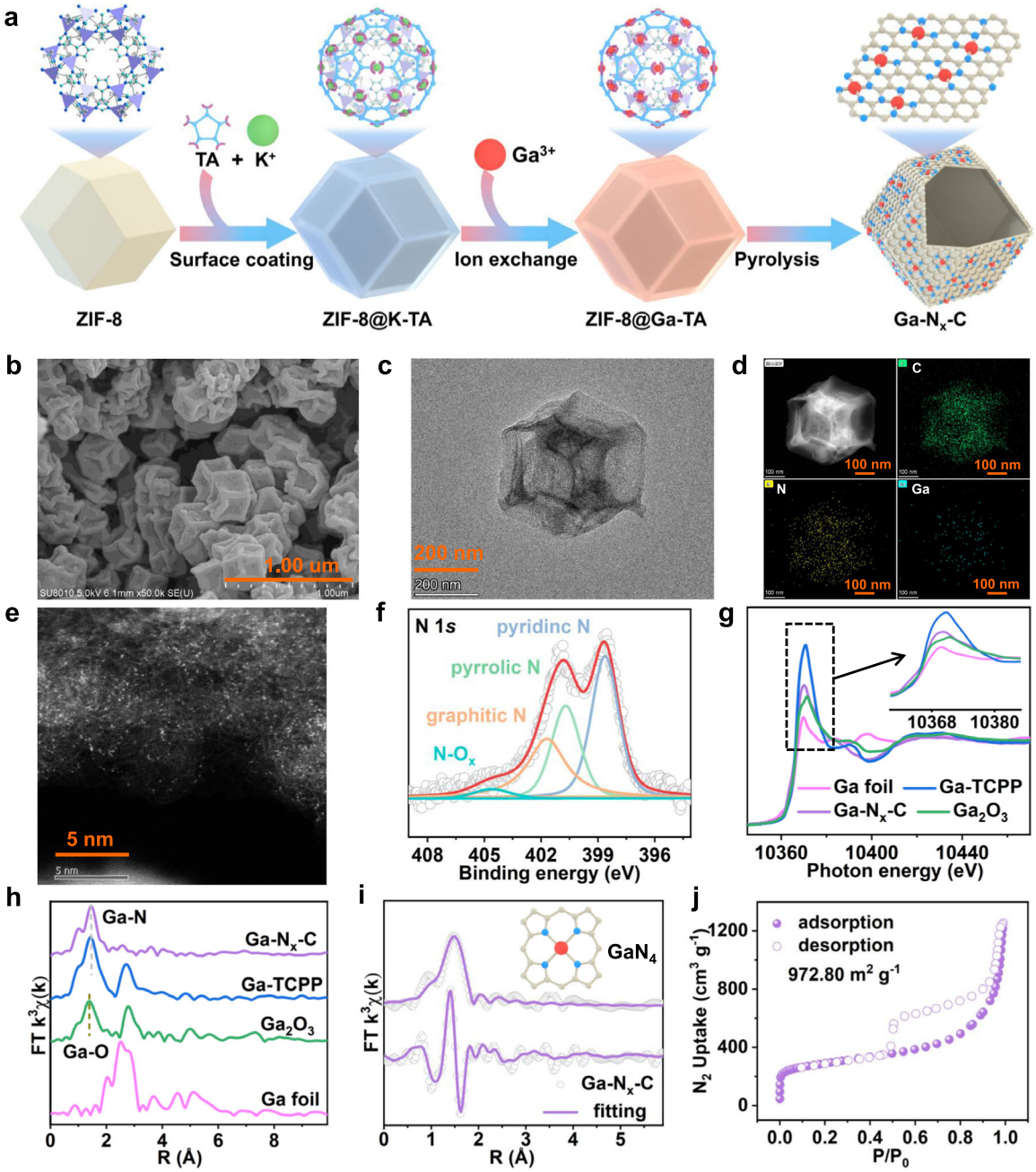

Fig. 2 | The synthesis and structural characterization of Ga-N_x-C. a Schematic illustration of the synthesis of Ga-N_x-C. **b**, **c** SEM and TEM images of Ga-N_x-C. **d** HAADF-STEM images and corresponding EDS maps revealing a homogeneous distribution of C (green), N (yellow), and Ga (blue) in Ga-N_x-C. **e** Aberration-corrected HAADF-STEM image of Ga-N_x-C, showing the atomically dispersed gallium. **f** N 1*s* XPS spectrum for Ga-N_x-C. **g** Ga K-edge XANES spectra (inset: expanded view showing the Ga valence states). **h** FT k^3-weighted $\chi(k)$ EXAFS spectra. **i** EXAFS fitting curves for Ga-N_x-C. **j** N_2 adsorption-desorption isotherms for Ga-N_x-C.

the crystalline texture of the parent ZIF-8 nanocrystals, as confirmed by powder X-ray diffraction (PXRD) and Fourier transform infrared (FT-IR) spectroscopy (Supplementary Figs. 1 and 2). Scanning electron microscopy (SEM) revealed ZIF-8@Ga-TA retained the characteristic polyhedral morphology of ZIF-8 (Supplementary Fig. 3). Subsequently, hollow Ga-N_x-C capsules were obtained by pyrolysis of ZIF-8@Ga-TA under an argon atmosphere.

SEM and transmission electron microscopy (TEM) images revealed that the Ga-N_x-C capsules consisted of very thin carbon layers (Fig. 2b, c). High-angle annular dark-field scanning transmission electron microscopy (HAADF-STEM) and corresponding energy dispersive spectroscopy (EDS) elemental mapping images showed that C, N, and Ga were distributed uniformly in Ga-N_x-C (Fig. 2d). Moreover, atomically dispersed gallium sites were evidenced in the aberration-corrected HAADF-STEM images (Fig. 2e), which showed bright spots of atomic size. X-ray photoelectron spectroscopy (XPS) analysis of Ga-N_x-C verified the presence of C, N, and Ga in the sample (Supplementary Fig. 4). The N 1*s* spectrum was deconvoluted into pyridinic N (398.6 eV), pyrrolic N (400.7 eV), graphitic N (401.7 eV), and oxidized-N (404.7 eV) species (Fig. 2f)[28,33].

Next, X-ray absorption near-edge structure (XANES) and Fourier-transformed extended X-ray absorption fine structure (EXAFS) measurements were conducted on Ga-N_x-C to determine the valence state and the local coordination environment of the atomically dispersed gallium species. Ga foil, Ga_2O_3, and gallium(III)-(4-methoxycarbonylphenyl) porphyrin (Ga-TCPP) were used as reference

samples[34]. As shown in Ga K-edge XANES spectra, the absorption edge position for Ga-N_x-C was located between the Ga foil and Ga_2O_3, suggesting the valence state of Ga in Ga-N_x-C was between 0 and +3 (Fig. 2g). Furthermore, the absorption edge of Ga-N_x-C was close to that of Ga-TCPP, suggesting the valence state of Ga in Ga-N_x-C was likely between +2 and +3. Possibly, some of the Ga(III) ions in ZIF-8@Ga-TA were reduced to Ga(II) during high-temperature pyrolysis step used to synthesize Ga-N_x-C. EXAFS showed that Ga-N_x-C and Ga-TCPP both had peaks at ~1.46 Å, which could readily be assigned to a Ga-N scattering path (Fig. 2h). Both pyridinic N and pyrrolic N can bind gallium ions, forming porphyrin-like GaN_4 sites on the capsules. The peak at ~2.7 Å for Ga-TCPP was attributed to a metal-carbon (i.e., Ga-C) second shell of the porphyrinic ring[34]. The wavelet transform (WT) EXAFS plot of Ga-N_x-C showed the maximum at R(~1.46 Å)/k(~4.38 Å), which could be assigned to Ga-N bonding (Supplementary Fig. 5). No obvious peak due to Ga-Ga bonding was observed, indicating the absence of gallium nanoparticles. The fitting results confirmed a Ga-N coordination number ~4, consistent with the porphyrin-like GaN_4 structure (Fig. 2i and Supplementary Table 2). The porosity of Ga-N_x-C was determined by N_2 sorption at 77 K. The adsorption-desorption isotherms were type IV with an obvious adsorption/desorption hysteresis at higher P/P_0 values, suggesting a hierarchical porous structure with abundant mesopores (Fig. 2j). The calculated Brunauer-Emmett-Teller (BET) surface area of Ga-N_x-C was 972.80 $m^2 g^{-1}$. A pore size distribution analysis using the nonlocal density functional theory (NLDFT) method afforded an average pore size centered at 15 nm (Supplementary Fig. 6). Ga-N_x-C contained 1.29 wt.% gallium, as determined by inductively coupled plasma mass spectrometry (ICP-MS). Porous N-doped carbons supporting atomically dispersed gallium catalysts have been shown previously to offer excellent electrocatalytic performance in reactions such as the carbon dioxide reduction reaction[35]. Therefore, we hypothesized that the developed Ga-N_x-C capsules should be efficient catalysts for the electrocatalytic reduction/extraction of uranium from aqueous solution.

Electrochemical uranium extraction performance

Uranium extraction from mining waste, nuclear waste, seawater, and contaminated water remains an attractive proposition for both nuclear fuel supply and environmental remediation[16,36–39]. Electrochemical uranium extraction methods are regarded as a promising alternative to traditional chemical processing methods for U extraction and recycling. Although enormous efforts have been focused on this aspect, until now there have been no reports of the electrochemical generation of U(IV) solids such as UO_2 under ambient conditions. In this light, we set about exploring the electrochemical uranium extraction properties of Ga-N_x-C under various conditions.

We first tested the U(VI) redox properties of Ga-N_x-C capsules by running cyclic voltammetry (CV) in uranium-spiked groundwater (~500 ppm). Ga-N_x-C loaded on carbon felt was used as the working electrode. Ag/AgCl and graphite rod were used as reference and counter electrodes, respectively. A reduction peak of U(VI) is observed at a potential (V vs. Ag/AgCl) of −0.41 V, indicating that U(VI) was reduced to U(IV) (Fig. 3a). No U(VI) reduction peaks were observed in the absence of Ga-N_x-C (Fig. 3b). Subsequently, we studied the uranium extraction performance of Ga-N_x-C using a square wave conversion method in ~1.2 ppm and ~120 ppb uranium-spiked groundwater. The uranium concentration was reduced from ~1.2 ppm (and ~120 ppb) to lower than 13 ppb (and 3 ppb) in 1440 min, suggesting a high removal efficiency (Fig. 3c, d). The extraction capacities of Ga-N_x-C were calculated to be 22.63 and 2.36 mg g^{-1}, respectively. Notably, 27.6% and 38.2% calcium removal were detected in ~1.2 ppm and ~120 ppb uranium-spiked groundwater, respectively. The magnesium concentration was reduced from ~5.1 ppm to 2.1 ppm (removal percentage of 58.9%) and 2.254 ppm (removal percentage of 55.8%) under the same conditions. To further investigate the generation products through electrocatalysis, we performed extraction experiments in ~20 ppm uranium-spiked groundwater. As shown in Fig. 3e, some pale yellow products formed on the working electrode during electrocatalysis in ~20 ppm uranium-spiked groundwater. These pale yellow products were collected and examined by PXRD, SEM, and XPS, revealing the generation of $CaCO_3$ nanosheets and $Mg(OH)_2$ nanosheets attached to the Ga-N_x-C capsules (Fig. 3f, g and Supplementary Fig. 7). Besides Na, K, Zn, Mg, and Ga metals, the XPS spectrum showed the presence of uranium after electrocatalysis (Supplementary Fig. 7). The U 4*f* XPS spectrum of the pale yellow products showed U $4f_{7/2}$ and U $4f_{5/2}$ peaks at 381.6 and 392.3 eV, respectively, corresponding to a U(IV) species (Fig. 3h)[15]. No UO_2 signals were observed by PXRD, which might be due to the small size of the nanoparticles. However, we observed peaks due to UO_2 nanocrystals in the PXRD pattern of the pale yellow product from ~50 ppm uranium-spiked groundwater (Supplementary Fig. 8). We further carried out high-resolution TEM (HRTEM) measurements to analyze the components in the pale yellow products. HRTEM images of some of the larger particles revealed lattice fringes with interplanar distances of around 3.0 Å and 2.3 Å, which were assigned to the (104) planes of $CaCO_3$ and (101) planes of $Mg(OH)_2$, respectively (Supplementary Fig. 9). Moreover, some dark-color nanoparticles with a diameter of ~6–7 nm were observed, showing lattice spacings of 3.2 Å, which can be assigned to the (111) plane of face-centered cubic UO_2 nanoparticles (Fig. 3i)[15]. No solid products were obtained when performing experiments in uranium-spiked deionized water under similar conditions (Supplementary Fig. 10). These results indicate that U(VI) was reduced to U(IV) in the presence of Ca(II), Mg(II), or other metal ions in the groundwater, which appeared to promote the formation of solid UO_2.

The above results inspired us to further investigate the effects of secondary metal ions on uranium extraction from aqueous solutions. Next, electrocatalytic extraction of uranium experiments were conducted using deionized water containing uranium and one type of secondary metal ion. Initially, CV tests were conducted on Ga-N_x-C to study the reduction voltage of U(VI) in aqueous solution in the presence of each different type of metal ion. The obtained U(VI) reduction voltages were used for uranium extraction studies in the presence of the different metal ions (Supplementary Fig. 11). In the presence of Na^+, K^+, or Cs^+ ions, no solid was obtained after 24 h electrocatalysis, suggesting that U(VI) was not reduced to U(IV) during catalysis (Fig. 4a and Supplementary Fig. 12). XANES revealed that the valence state of the uranium adsorbed on the Ga-N_x-C electrode surface was +6 in all these solutions (Fig. 4b)[15,40]. EXAFS and corresponding fitting results matched data for $UO_2(NO_3)_2{\cdot}6H_2O$, suggesting no U(IV) product was generated in aqueous solutions containing alkali metal ions (Fig. 4c and Supplementary Fig. 13).

We further conducted experiments in Mg^{2+}, Ca^{2+}, Sr^{2+}, Ba^{2+}, Cd^{2+} and Pb^{2+} aqueous solutions containing uranium. Pale yellow solids were obtained after electrocatalysis for all these ions (Supplementary Fig. 14). PXRD showed that $Mg(OH)_2$, $CaCO_3$, $SrCO_3$, $BaCO_3$, $CdCO_3$, and $PbCO_3$ were obtained, respectively (Fig. 4d and Supplementary Fig. 15). No uranium-containing crystalline solid was detected in the presence of Mg^{2+}, Ca^{2+}, Sr^{2+}, or Ba^{2+}, indicating the formation of amorphous or nanosized uranium-containing particles. UO_2 peaks were detected in uranium-spiked cadmium nitrate and uranium-spiked lead nitrate solutions (Fig. 4d). XANES and EXAFS spectra confirmed the existence of UO_2 in these products, conclusively demonstrating that U(VI) could be electrocatalytically reduced to U(IV)O_2 in the presence of these metal ions (Fig. 4e, f and Supplementary Fig. 16). Notably, the UO_2 peaks were detected by PXRD for experiments conducted in the presence of Cd^{2+} or Pb^{2+} ions, further supporting these conclusions (Fig. 4d and Supplementary Fig. 15).

Next, the electrocatalytic experiments were carried out in aqueous Ni^{2+}, Zn^{2+}, Al^{3+}, and Fe^{3+} solutions. Metallic nickel, zinc oxide, Fe-containing and Al-containing amorphous solids were obtained after

https://doi.org/10.1038/s41467-024-52083-1

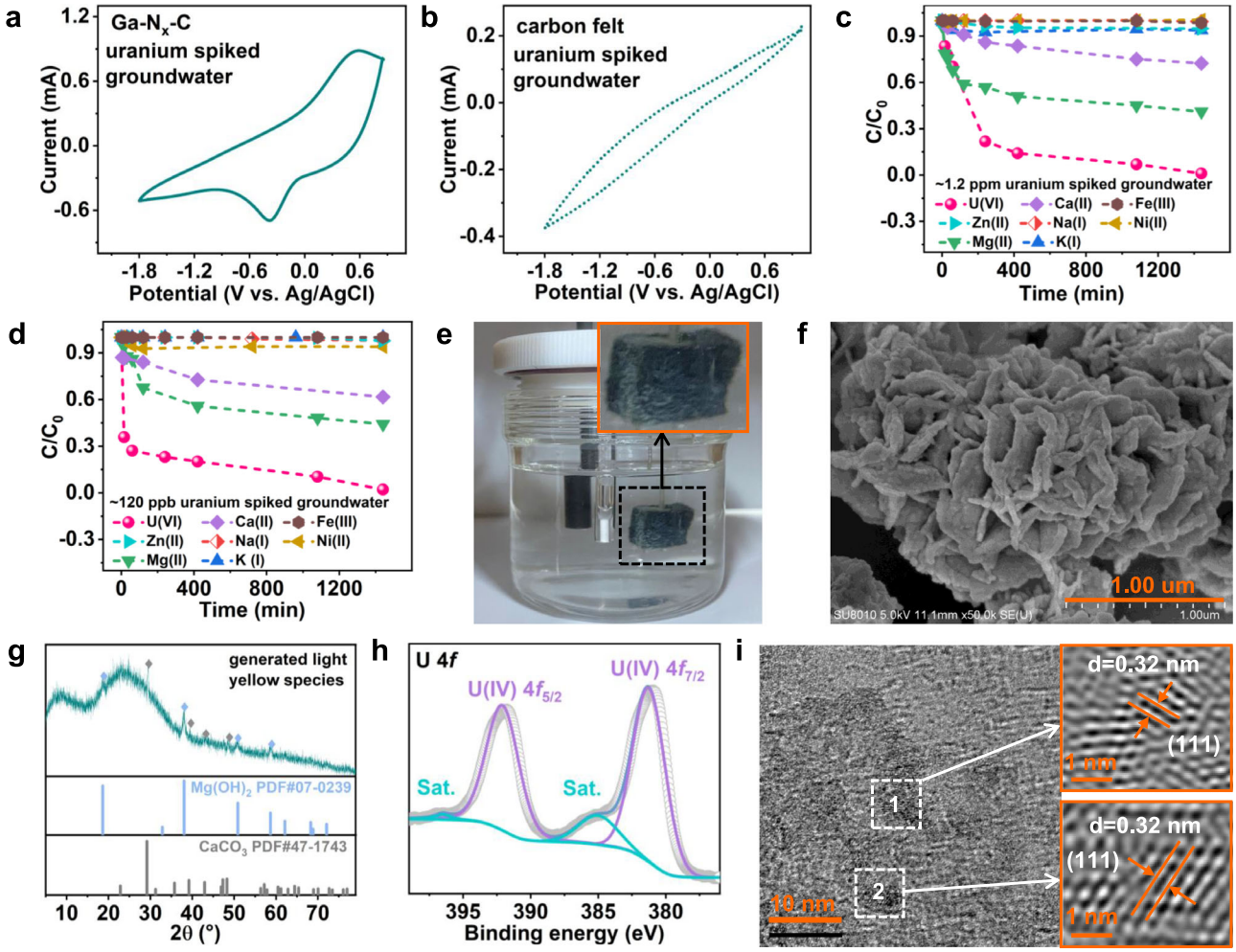

Fig. 3 | Electrochemical uranium removal performance of Ga-N_x-C in uranium-spiked groundwater and product analysis. a, **b** Cyclic voltammograms of Ga-N_x-C/carbon felt and carbon felt (blank) in uranium-spiked groundwater (~500 ppm). **c**, **d** Uranium extraction from spiked groundwater with initial uranium concentrations of ~1.2 ppm and ~120 ppb using Ga-N_x-C. **e** Photograph showing the generated pale yellow product formed through electrocatalysis in ~20 ppm uranium-spiked groundwater (inset: expanded view showing the working electrode). **f** SEM image of the pale yellow product formed through electrocatalysis in ~20 ppm uranium-spiked groundwater. **g** PXRD for the pale yellow product formed through electrocatalysis in ~20 ppm uranium-spiked groundwater. **h** U 4*f* XPS spectrum of the pale yellow product formed through electrocatalysis in ~20 ppm uranium-spiked groundwater. **i** HRTEM images of UO_2 nanoparticles generated through electrocatalysis in ~20 ppm uranium-spiked groundwater (inset: expanded view showing the lattice spacing.).

electrocatalytic reduction, as revealed by PXRD analysis (Supplementary Fig. 17). The formation of UO_2 species was verified by XANES and EXAFS spectra (Supplementary Fig. 18).

We next studied the effects of lanthanide and actinide metal ions such as Ce^{4+}, La^{3+}, Eu^{3+}, and Th^{4+} ions. Interestingly, a crystalline bimetallic oxide phase, $Ce_{0.8}U_{0.2}O_2$, was generated in the presence of Ce^{4+} ions[41]. The PXRD showed peaks at 28.8°, 33.3°, 47.7°, 56.6°, and 76.9°, corresponding to (111), (200), (220), (311), and (331) reflections of $Ce_{0.8}U_{0.2}O_2$ (Fig. 4g). The HRTEM image of the $Ce_{0.8}U_{0.2}O_2$ product showed lattice fringes with an interplanar spacing of 3.1 Å, which matched the contrast profiles of the (111) planes (Fig. 4h). To further probe the electronic structure of the $Ce_{0.8}U_{0.2}O_2$ product, XANES and EXAFS measurements were performed. The U L_3-edge XANES spectrum of $Ce_{0.8}U_{0.2}O_2$ was similar to that of the UO_2 standard sample, with the edge position being typical for U(IV) (Supplementary Fig. 19). Further, the EXAFS spectrum exhibited main peaks at 1.04 Å and 1.42 Å, corresponding to the first and second U-O coordination shells in $Ce_{0.8}U_{0.2}O_2$, respectively (Supplementary Fig. 19). Fitting the EXAFS data to the $Ce_{0.8}U_{0.2}O_2$ structural model was successful (fitting results indicated that the U atoms were coordinated by four O atoms, Fig. 4i). When experiments were carried out in aqueous La^{3+}, Eu^{3+}, or Th^{4+} solutions, amorphous powder products were obtained, evidenced by PXRD measurements (Supplementary Fig. 20). XANES and EXAFS analysis revealed a similar U(IV) structural model to that of the $Ce_{0.8}U_{0.2}O_2$ (Supplementary Fig. 19). Annealing of amorphous samples is a well-known method to synthesize larger crystallites, thereby giving sharper and more intense PXRD peaks. Therefore, we further annealed each amorphous sample at 800 °C in a nitrogen atmosphere to verify the presence of bimetallic metal oxides. As expected, the PXRD patterns for the annealed samples revealed the presence of crystalline $Eu_{0.76}U_{0.43}O_2$, $La_{0.9}U_{0.3}O_2$, and $Th_{0.75}U_{0.25}O_2$ (Supplementary Fig. 20)[41–43].

In-situ Raman spectroscopy was next applied to gain deeper understanding of the electrocatalytic processes leading to the generation of $Ce_{0.8}U_{0.2}O_2$ in Ce^{4+}/UO_2^{2+} aqueous solutions. K^+/UO_2^{2+} aqueous solution was used for comparison. Before square wave potential cycling, U(VI) signals was detected at 870 cm^{-1} that could be assigned to adsorbed UO_2^{2+} ions (Fig. 5a)[44,45]. As the reaction time increased, new signals appeared at 257 cm^{-1} and 743 cm^{-1} suggesting the generation of U(IV)[44,45]. No U(IV) signals were observed in the presence of K^+ (Fig. 5b). These results indicated that the U(VI) was reduced to U(IV) in the presence of Ce^{4+} ions (and by analogy La^{3+}, Eu^{3+}, and Th^{4+} ions) leading to the generation of bimetallic metal oxides, consistent with the X-ray absorption spectroscopy (XAS) and PXRD results.

https://doi.org/10.1038/s41467-024-52083-1

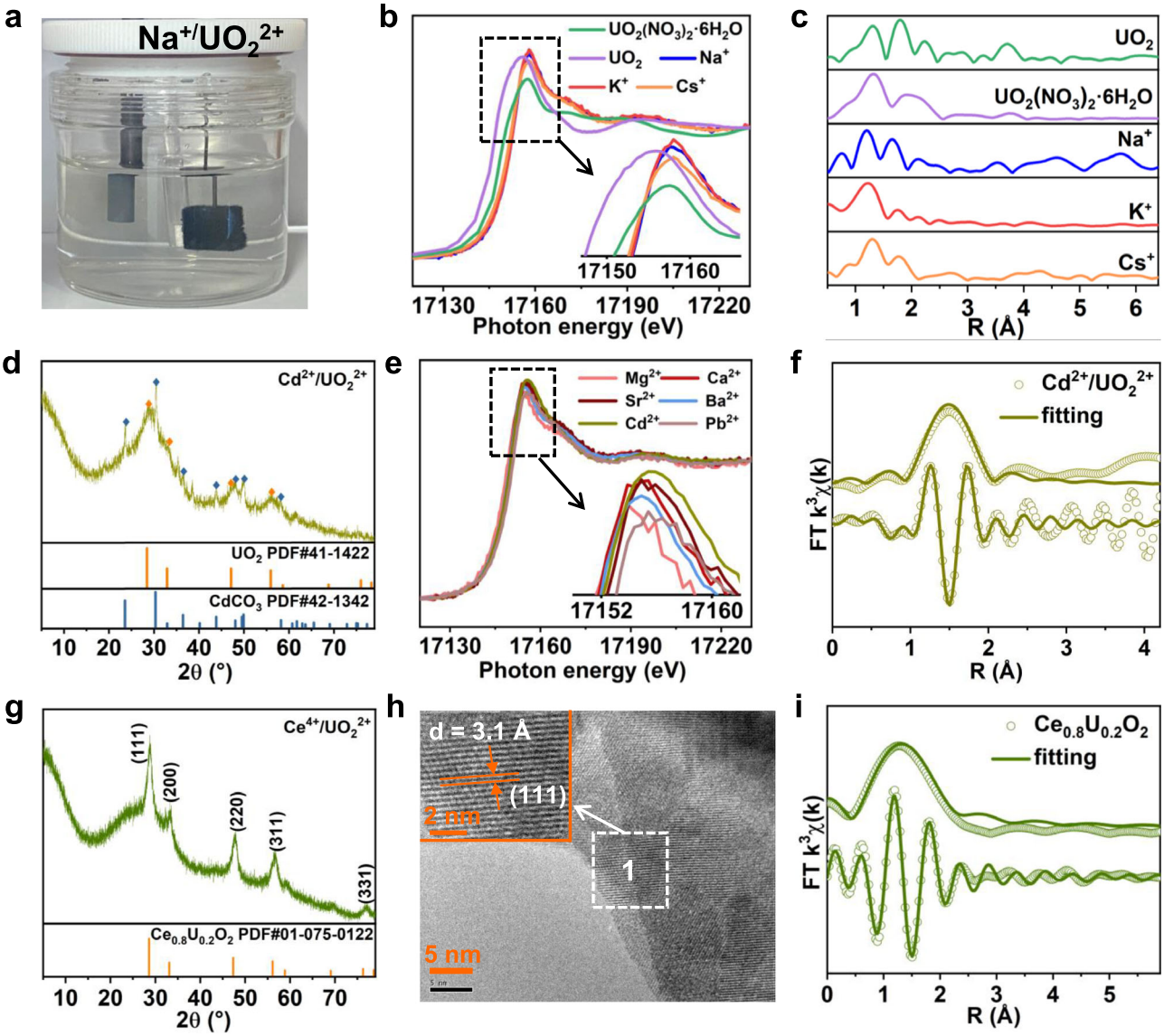

Fig. 4 | Product analysis for the electrochemical reduction of U(VI) by Ga-N_x-C in solutions containing selected secondary metal ions. a Photograph showing no solids were generated through electrocatalysis on Ga-N_x-C in ~100 ppm uranium-spiked sodium nitrate solution. **b**, **c** U L_3-edge XANES and EXAFS spectra of Ga-N_x-C after electrocatalytic uranium extraction in the presence of Na^+, K^+, or Cs^+ ions (**b** inset: expanded view showing the U valence states). **d** PXRD pattern of the electrocatalytically generated products in ~100 ppm uranium-spiked cadmium nitrate solution. **e** U L_3-edge XANES spectra of Ga-N_x-C after electrocatalytic uranium extraction in the presence of Mg^{2+}, Ca^{2+}, Sr^{2+}, Ba^{2+}, Cd^{2+}, or Pb^{2+} ions (inset: expanded view showing the U valence states). **f** U L_3-edge EXAFS curves and fitting results for Ga-N_x-C after uranium extraction in ~100 ppm uranium-spiked cadmium nitrate solution. **g** PXRD pattern of electrocatalytically generated $Ce_{0.8}U_{0.2}O_2$. **h** HRTEM image of electrocatalytically generated $Ce_{0.8}U_{0.2}O_2$ (inset: expanded view showing the lattice spacing). **i** U L_3-edge EXAFS curves and fitting results for electrocatalytically generated $Ce_{0.8}U_{0.2}O_2$. The reference data for UO_2 and $UO_2(NO_3)_2{\cdot}6H_2O$ in (**b**, **c**) were taken from our previous work[28].

On the basis of these findings, we then performed electrocatalytic uranium extraction studies using Ga-N_x-C in a simulated low and media level radioactive waste (LMW) solution[46,47]. As shown in Fig. 5c, Ga-N_x-C capsules could rapidly remove uranium in the simulated LMW solution, achieving a removal capacity of 1015.9 mg g^{-1} in 48 h. Notably, the Ce^{4+} was also quickly removed as the UO_2^{2+} was consumed. The concentrations of other metal ions in the LMW solution were barely affected by electrocatalysis (Fig. 5d). The PXRD pattern of the generated powder showed peaks matching $Ce_{0.8}U_{0.2}O_2$, suggesting that the reduced U(IV) has an exceptional binding affinity towards Ce^{4+} relative to other ions (Fig. 5e). The SEM image showed that Ga-N_x-C retained its hollow capsule morphology, indicating good structure stability (Fig. 5f and Supplementary Fig. 21). XPS revealed that Ga, N, and C were retained on the surface of Ga-N_x-C after catalysis, further confirming its good stability (Fig. 5g and Supplementary Fig. 22). We further investigated the electrochemical durability of Ga-N_x-C in a large-scale extraction experiment using 50 L of uranium spiked groundwater (~1 ppm). A uranium extraction capacity of 2.23 g g^{-1} was achieved after 108 h, suggesting Ga-N_x-C would be a very promising electrocatalyst for uranium extraction from contaminated groundwater (Fig. 5h, i).

Electrochemical mechanism studies

On the basis of the above findings, we next explored mechanism of U(IV) oxide (including UO_2 and bimetallic $M_xU_yO_2$, M = Ce, Th, La, Eu) formation using molecular dynamics (MD) simulations[48]. Since electrocatalysis generates the UO_2 in the presence of alkaline earth metal ions and transition metal ions, whilst yielding $M_xU_yO_2$ in the presence of lanthanide and actinide metal ions, we first studied the dynamic interactions between U(IV) and selected representative secondary metal ions (such as K^+, Ca^{2+}, Fe^{3+}, or Ce^{4+}) in aqueous solutions.

https://doi.org/10.1038/s41467-024-52083-1

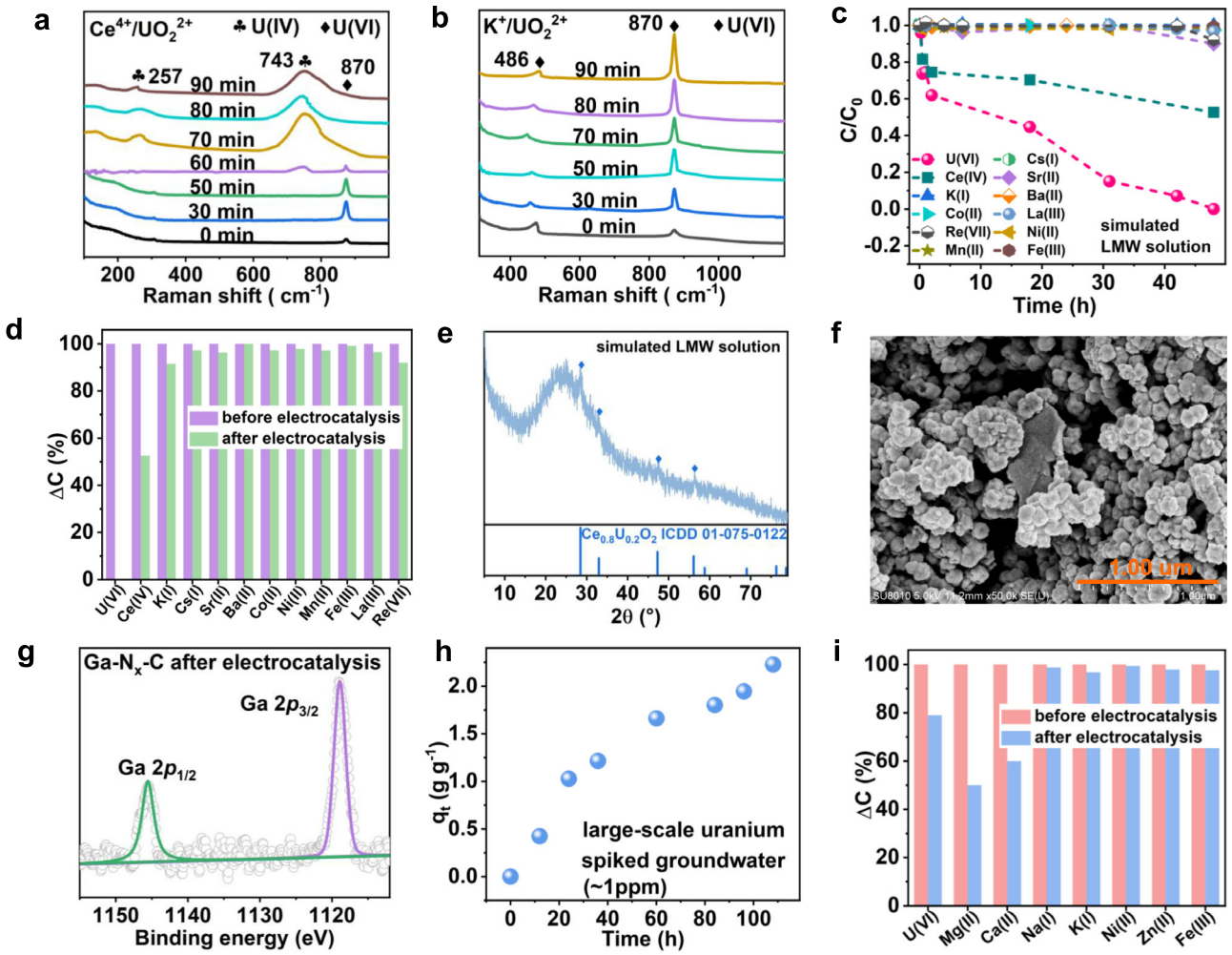

Fig. 5 | Electrochemical removal of uranium by Ga-N_x-C in a simulated LMW solution. **a** In situ Raman spectra collected from a Ga-N_x-C/carbon felt working electrode in ~100 ppm uranium-spiked cerous nitrate solution. **b** In situ Raman spectra collected from the Ga-N_x-C/carbon felt working electrode in ~100 ppm uranium-spiked potassium nitrate solution. **c** Uranium extraction under LMW conditions, using Ga-N_x-C as an electrocatalyst. **d** Concentration changes of various ions before and after uranium extraction under LMW conditions, using Ga-N_x-C as the electrocatalyst. **e** PXRD pattern of the electrocatalytically generated products under LMW conditions. **f** SEM image of Ga-N_x-C after uranium extraction under LMW conditions. **g** Ga 2*p* XPS spectrum after uranium extraction under LMW conditions. **h** Large-scale extraction of uranium from spiked groundwater by the Ga-N_x-C electrocatalyst. **i** Concentration changes of various ions before and after uranium extraction from spiked groundwater, using Ga-N_x-C as the electrocatalyst.

Figure 6a shows the snapshots from the MD simulations in the presence of K^+, NO_3^-, and H_2O molecules. Initially, K^+ and U(IV) were uniformly dispersed in the aqueous solution. No aggregation of K^+ and U(IV) were observed after 100 ps or 500 ps, suggesting a very weak interaction between K^+ and U(IV). The corresponding radial distribution functions (RDFs) through the MD simulation revealed the interactions between U(IV) and NO_3^- or H_2O molecules were much stronger than with K^+ (Fig. 6b). Moreover, mean square displacement (MSD) analysis showed that the diffusion coefficients of K^+ and U(IV) differed significantly, thus allowing re-oxidation of the generated U(IV) to U(VI). Thus, no solid U(IV) products formed (Fig. 6c). This helps to explain why no UO_2 or $M_xU_yO_2$ were generated in the presence of alkali metal ions. In contrast, U(IV) and Ca^{2+} aggregated after 100 ps, and the aggregation intensified after 500 ps (Fig. 6d). Compared to K^+, RDFs showed similar diffusion coefficients for U(IV) and Ca^{2+}, as well as stronger interactions, which likely facilitated the co-generation of UO_2 and $CaCO_3$ precipitates during electrocatalysis (Fig. 6e, f). Furthermore, similar results were obtained in the presence of Fe^{3+}, with even stronger interactions between U(IV) and Fe^{3+} (Fig. 6g–i). Notably, U(IV) and Ce^{4+} aggregated within a very short period of time, with the emergence of a very sharp and intense peak at *r* ~3.7 Å by RDFs reflecting a very strong interaction between the two ions (Fig. 6j–l). Figure 6c, f, i, l and Supplementary Fig. 23 show the corresponding diffusion coefficient plots and relative concentration distribution analysis for the U(IV)/K^+, U(IV)/Ca^{2+}, U(IV)/Fe^{3+}, and U(IV)/Ce^{4+} systems. The diffusion coefficient gap and relative concentration difference between U(IV) and K^+ gradually increased, while very similar diffusion coefficients and relative concentrations were seen for U(IV)/Ca^{2+}, U(IV)/Fe^{3+}, and U(IV)/Ce^{4+} during the electrocatalysis process. Again, the data suggested that Ca^{2+}, Fe^{3+} and Ce^{4+} ions promote the generation of UO_2 or $U_xM_yO_2$ in the aqueous solutions. The MD simulations provide theoretical justification for the production of UO_2 and $U_xM_yO_2$ solids in the presence of certain secondary metal ions.

Discussion

Taken together, the above results validate our secondary metal ion-induced strategy for electrocatalytic generating stable U(IV) solid products (such as UO_2 and $U_xM_yO_2$) in the presence of specific secondary metal ions. The secondary metal ions demonstrate distinctive interactions with U(IV) in the aqueous solution. For example, the presence of alkaline earth metal ions or transition metal ions promote the generation of UO_2 solid. The presence of lanthanide or actinide

https://doi.org/10.1038/s41467-024-52083-1

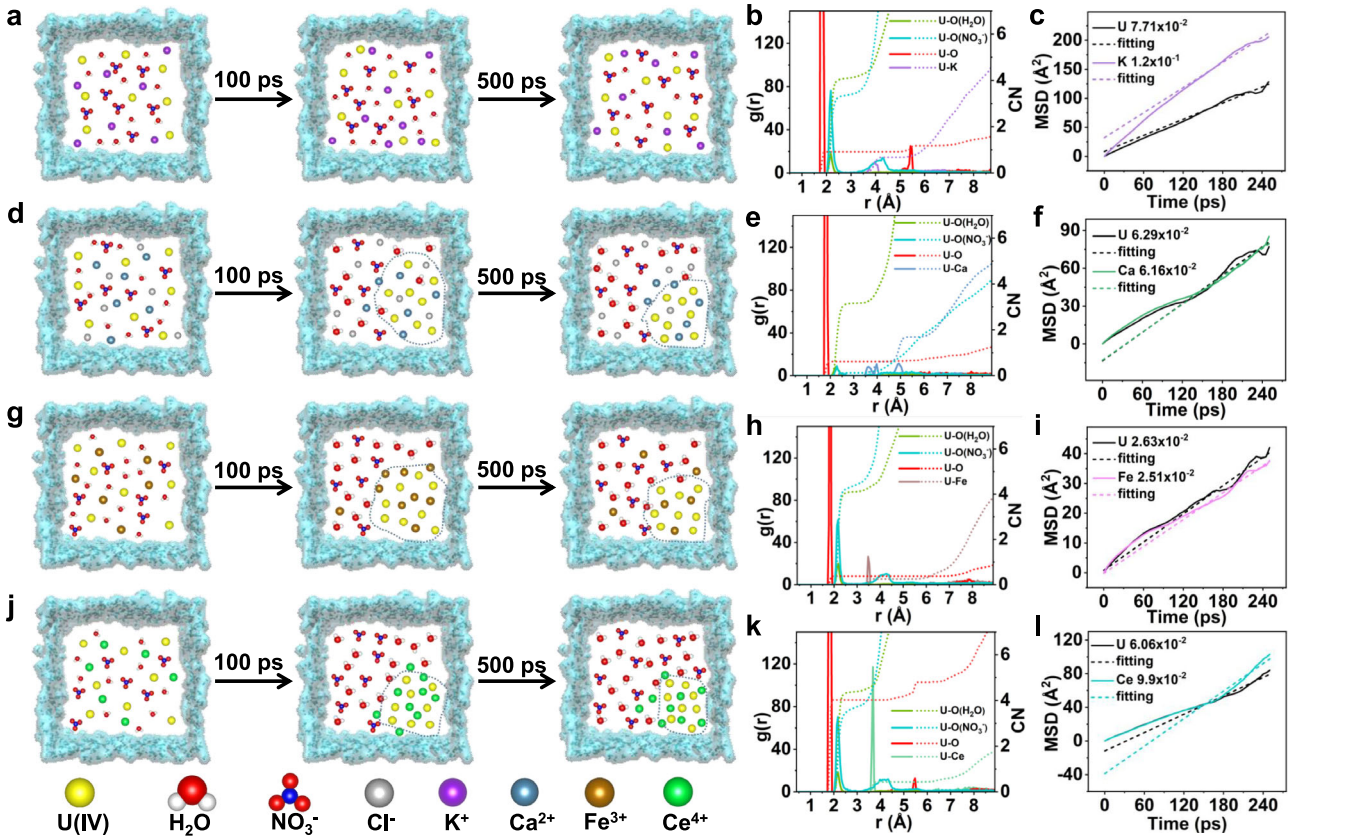

Fig. 6 | Mechanism analysis of secondary metal ion-induced electrochemical U(VI) reduction to U(IV) solid products. a Selected snapshots from the MD simulation showing the K^+/U(IV) interactions on Ga-N_x-C in ~100 ppm uranium-spiked potassium nitrate solution. **b** RDFs plots of U(IV)-K^+, U(IV)-O, U(IV)-O(H_2O), and U(IV)-O(NO_3^-), and their corresponding average coordination number. **c** MSD-time curves for the transport of U(IV)/K^+ (showing the different diffusion coefficients). **d** Selected snapshots from the MD simulation showing the Ca^{2+}/U(IV) interactions on Ga-N_x-C in ~100 ppm uranium-spiked calcium chloride solution. **e** RDFs plots of U(IV)-Ca^{2+}, U(IV)-O, U(IV)-O(H_2O), and U(IV)-O(NO_3^-), and their corresponding average coordination number. **f** MSD-time curves for the transport of U(IV)/Ca^{2+}. **g** Selected snapshots from the MD simulation showing the Fe^{3+}/U(IV) interactions on Ga-N_x-C in ~100 ppm uranium-spiked ferric nitrate solution. **h** RDFs plots of U(IV)-Fe^{3+}, U(IV)-O, U(IV)-O(H_2O), and U(IV)-O(NO_3^-), and their corresponding average coordination number. **i** MSD-time curves for the transport of U(IV)/Fe^{3+}. **j** Selected snapshots from the MD simulation showing the Ce^{4+}/U(IV) interactions on Ga-N_x-C in ~100 ppm uranium-spiked cerous nitrate solution. **k** RDFs plots of U(IV)-Ce^{4+}, U(IV)-O, U(IV)-O(H_2O), and U(IV)-O(NO_3^-), and their corresponding average coordination number. **l** MSD-time curves for the transport of U(IV)/Ce^{4+}.

ions, which possess stronger interactions with U(IV), lead to the generation of bimetallic oxides. These findings challenge the existing paradigm that U(IV) solid products cannot be electrocatalytically generated from aqueous U(VI) under ambient conditions. We further identified the functional relationship between the type of secondary metal ions and U(IV) solid product formed. Further, the Ga-N_x-C catalyst showed excellent electrocatalytic reduction activities, resulting in efficient U(VI) extraction from contaminated groundwater and LMW solutions.

In summary, we report the electrocatalytic synthesis of U(IV) solid products from aqueous solutions containing uranyl ions and various secondary metals. In the presence of alkaline earth metal ions (such as Mg^{2+}, Ca^{2+}, Sr^{2+}, and Ba^{2+}) and transition metal ions (such as Ni^{2+}, Zn^{2+}, Al^{3+}, Fe^{3+}, Cd^{2+}, and Pb^{2+}), a Ga-N_x-C catalyst generated solid UO_2. In the presence of lanthanide and actinide metal ions (such as Ce^{4+}, La^{3+}, Eu^{3+}, and Th^{4+}), bimetallic oxides formed (such as $Ce_{0.8}U_{0.2}O_2$, $Eu_{0.76}U_{0.43}O_2$, $La_{0.9}U_{0.3}O_2$, and $Th_{0.75}U_{0.25}O_2$). The electrocatalytic uranium extraction method reported here is suitable for uranium extraction from contaminated groundwater and simulated LMW solutions, with strength of the interaction between U(IV) and the secondary in controlling the type of U(IV) solid produced. To the best of our knowledge, this study to report the generation of UO_2 and $M_xU_yO_2$ via electrochemical uranium extraction under ambient conditions would arouse broad interest. This work is expected to have far-reaching implications for the extraction/recycling of uranium resources and environmental remediation.

Methods

Materials and measurements

All chemicals were sourced from commercial suppliers and used without further purification. Zinc nitrate hexahydrate ($Zn(NO_3)_2{\cdot}6H_2O$, 99% purity), gallium nitrate hydrate ($Ga(NO_3)_3{\cdot}xH_2O$, 99.99% purity), uranyl nitrate hexahydrate ($UO_2(NO_3)_2{\cdot}6H_2O$, 99% purity), sodium nitrate ($NaNO_3$, 99% purity), potassium nitrate (KNO_3, 98.5% purity), cesium nitrate ($CsNO_3$, 99% purity), magnesium chloride ($MgCl_2$, 98% purity), calcium chloride ($CaCl_2$, 99.9% purity), strontium nitrate ($Sr(NO_3)_2$, 99.5% purity), barium nitrate ($Ba(NO_3)_2$, 99.5% purity), nickel chloride hexahydrate ($NiCl_2{\cdot}6H_2O$, 99%), zinc chloride ($ZnCl_2$, 98% purity), cadmium nitrate tetrahydrate ($Cd(NO_3)_2{\cdot}4H_2O$, 99% purity), lead nitrate ($Pb(NO_3)_2$, 99% purity), iron(III) nitrate nonahydrate ($Fe(NO_3)_3{\cdot}9H_2O$, 98.5% purity), aluminum nitrate nonahydrate ($Al(NO_3)_3{\cdot}9H_2O$, 99% purity), cerium nitrate hexahydrate ($Ce(NO_3)_4{\cdot}6H_2O$, 99.9% purity), thorium nitrate hydrate ($Th(NO_3)_4{\cdot}xH_2O$, 98% purity), lanthanum nitrate hydrate ($La(NO_3)_3{\cdot}6H_2O$, 99% purity), europium(III) nitrate hexahydrate ($Eu(NO_3)_3{\cdot}6H_2O$, 99.9% purity), tannic acid (TA, 98%), potassium hydroxide (KOH, 90% purity), 2-methylimidazole (98%) and methanol (MeOH, 99.5%) were purchased from Macklin Biochemical Technology Co., Ltd. The groundwater was collected in Mentougou, Beijing, China.

PXRD patterns were collected on a Rigaku SmartLab SE X-ray diffractometer equipped with a Cu K_α source. BET surface areas were determined from N_2 adsorption/desorption isotherms collected at 77 K using a Micromeritics TriStar II instrument. SEM images were recorded on Hitachi SU8010 and Regulus 8220 scanning electron microscopes. TEM images, HAADF-STEM images, and EDS elements maps were recorded on a JEM-2100F transmission electron microscopes operating at an accelerating voltage of 200 kV. High-resolution TEM (HRTEM) images were recorded on a JEM-2100 transmission electron microscope operating at an accelerating voltage of 200 kV. Aberration-corrected HAADF-STEM images were recorded on a JEM-ARM300F transmission electron microscope operating at an accelerating voltage of 300 kV. XPS analyses used a Thermo Scientific™ Nexsa™ spectrometer, equipped with a monochromatic Al K_α X-ray source (1486.6 eV). ICP-MS analyses were performed on an Agilent 7800 spectrometer. High-resolution Raman and in situ Raman spectra were recorded on a Jobin Yvon HR-800 Raman spectrometer equipped with a cobolt 05-01 series CW diode pumped laser (514 nm). CV analyses were conducted on a CHI 760 electrochemical workstation. All electrochemical uranium extraction experiments were performed using a square wave conversion method with a three-electrode electrochemical system under room temperature on a CHI 760 electrochemical workstation (Ag/AgCl and graphite rod were used as the reference electrode and counter electrode, respectively). Ga K-edge and U L_3-edge XAS data were collected in transmission mode at the Shanghai Synchrotron Radiation Facility (14 W station, SSRF).

Synthesis of ZIF-8, ZIF-8@K-TA, and ZIF-8@Ga-TA nanocrystals

ZIF-8 nanocrystals were synthesized using a reported procedure with a slight modification[31]. In a typical synthesis, 4.1 g of 2-methylimidazole was dissolved in 60 mL of MeOH to form a clear solution. Next, 1.68 g of $Zn(NO_3)_2{\cdot}6H_2O$ was then added into the 2-methylimidazole solution followed by vigorous stirring for 1 h. The mixture was then incubated at room temperature without stirring. After 24 h, the product was isolated as a white powder by centrifugation and washed several times with MeOH, and finally dried overnight under vacuum. Next, 300 mg of ZIF-8 nanocrystals were dispersed in deionized water by sonication for 10 min. Next, a tannic acid solution (24 mM, 10 mL) of pH = 8 (adjusted by adding aqueous 6 M KOH solution) was added to the ZIF-8 dispersion under constant stirring. After stirring for 5 min, the solid product was collected by centrifugation, washed several times with deionized water and MeOH, yielding ZIF-8@K-TA. Subsequently, 50 mg of gallium nitrate hydrate ($Ga(NO_3)_3{\cdot}xH_2O$) was dissolved in 150 mL of MeOH under stirring for 10 min. Then, the obtained ZIF-8@K-TA was added to the gallium nitrate solution, with the resulting dispersion being stirred for 3 h at room temperature. The solid product was collected by centrifugation and washed several times with MeOH. Finally, the product was dried in an oven at 40 °C under vacuum to yield ZIF-8@Ga-TA.

Synthesis of hollow Ga-N_x-C capsules

ZIF-8@Ga-TA was placed in a tube furnace and heated to 900 °C (3 °C min^{-1}) under an argon atmosphere. After annealing at 900 °C for 3 h, the powder sample was cooled to room temperature to give Ga-N_x-C capsules.

Electrochemical test

Electrochemical uranium extraction tests were performed on the CHI 760 electrochemical workstation. Ga-N_x-C/carbon felt, Ag/AgCl, and graphite rod were used as the working electrode, reference electrode, and counter electrode, respectively. 5 mg Ga-N_x-C was dispersed in a mixed solution of 1 mL ethanol and 50 uL Nafion, and ultrasonic uniformity, then added drop by drop on 1 cm × 1 cm × 1 cm carbon felt, and then dried in an infrared oven (~70 °C) for 12 h to prepare the working electrode (mass loading of catalyst ~5 mg cm^{-3}, ~4 wt.%). The electrochemical uranium extraction experiments were conducted in a quartz electrolytic cell with a volume of ~120 mL, a diameter of approximately 5 cm and a height of 6 cm.

Uranium extraction from spiked groundwater

The performance of Ga-N_x-C for the electrochemical extraction of uranium in uranyl-spiked groundwater was evaluated using CHI 760 electrochemical workstation. Ga-N_x-C/carbon felt, Ag/AgCl, and graphite rod were used as the working electrode, reference electrode, and counter electrode, respectively. The applied voltage was −0.8 V. The initial concentrations of uranium were ~120 ppb, ~1.2 ppm, and ~20 ppm. After electrocatalytic testing, the Ga-N_x-C/carbon felt working electrode was washed with distilled water and dried under vacuum at 60 °C to obtain the electrochemical product. At regular intervals, aliquots of the dispersion were removed and filtered through a 0.45 μm membrane filter. The concentration of U(VI) in the filtrates was measured using ICP-MS.

Electrochemical uranium extraction from deionized water containing uranium and one of the different secondary metal ions

The performance of Ga-N_x-C for the electrochemical extraction of uranium from deionized water containing uranium and a different secondary metal ion (such as Na^+, K^+, Cs^+, Mg^{2+}, Ca^{2+}, Sr^{2+}, Ba^{2+}, Ni^{2+}, Zn^{2+}, Cd^{2+}, Pb^{2+}, Fe^{3+}, Al^{3+}, Ce^{4+}, Th^{4+}, La^{3+}, Eu^{3+}) was evaluated using a square wave conversion method. Ga-N_x-C/carbon felt, Ag/AgCl, and graphite rod were used as the working electrode, reference electrode, and counter electrode, respectively. The applied voltage (determined by CV tests, Supplementary Fig. 11) are −0.8 V (Na^+), −0.8 V (K^+), (−0.8 V) Cs^+, −0.8 V (Mg^{2+}), −0.9 V (Ca^{2+}), −0.9 V (Sr^{2+}), −0.8 V (Ba^{2+}), −0.8 V (Ni^{2+}), −0.8 V (Zn^{2+}), −0.8 V(Cd^{2+}), −0.9 V (Pb^{2+}), −0.8 V (Fe^{3+}), −0.8 V (Al^{3+}), −1 V (Ce^{4+}), −1 V (Th^{4+}), −1 V (La^{3+}), −1 V (Eu^{3+}), respectively. The initial concentrations of uranium and secondary metal ions were both ~100 ppm with ~pH = 4.0. At regular intervals, aliquots of the dispersion were removed and filtered through a 0.45 μm membrane filter. After electrocatalytic testing, the Ga-N_x-C/carbon felt working electrode was washed with distilled water and dried under vacuum at 60 °C to obtain the electrochemical product. The concentration of U(VI) in the filtrates was measured on UV-spectrophotometry (SP-721E) and ICP-MS.

Electrochemical uranium extraction from simulated LMW solutions

The performance of the Ga-N_x-C for the electrochemical extraction of uranium from simulated LMW solution were evaluated using a square wave conversion method. Ga-N_x-C/carbon felt, Ag/AgCl, and graphite rod were used as the working electrode, reference electrode, and counter electrode, respectively. The applied voltage is −0.8 V. The initial concentrations of uranium were ~50 ppm. At regular intervals, aliquots of the dispersion were removed and filtered through a 0.45 μm membrane filter. After electrocatalytic testing, the Ga-N_x-C/carbon felt working electrode was washed with distilled water and dried under vacuum at 60 °C to obtained electrochemical product. The concentration of U(VI) in the filtrates was measured by ICP-MS.

Data availability

The authors declare that all the data supporting the findings of this study are available within the article (and Supplementary Information Files), or additional data are available from the corresponding author upon request. Source data are provided within this paper.

References

1. Deutch, J. Is net zero carbon 2050 possible? *Joule* **4**, 2237–2240 (2020).
2. Taylor, R. Reaction: a role for actinide chemists. *Chem* **1**, 662–663 (2016).

3. Gilbert, A. Q. & Bazilian, M. D. Can distributed nuclear power address energy resilience and energy poverty? *Joule* **4**, 1839–1843 (2020).
4. Wiechert, A. I., Yiacoumi, S. & Tsouris, C. The ocean's nuclear energy reserve. *Nat. Sustain.* **5**, 13–14 (2021).
5. Dai, S. Catalyst: challenges in development of adsorbents for recovery of uranium from seawater. *Chem* **7**, 537–539 (2021).
6. Kauffman, J. W., Laughlin, W. C. & Baldwin, R. A. Microbiological treatment of uranium mine waters. *Environ. Sci. Technol.* **20**, 243–248 (1986).
7. Gregory, K. B. & Lovley, D. R. Remediation and recovery of uranium from contaminated subsurface environments with electrodes. *Environ. Sci. Technol.* **39**, 8943–8947 (2005).
8. Kubatko, K.-A. H., Helean, B., Navrotsky, A. & Burns, P. C. Stability of peroxide-containing uranyl minerals. *Science* **302**, 1191–1193 (2003).
9. Yang, Q. et al. Uranium and radon in private bedrock well water in maine: geospatial analysis at two scales. *Environ. Sci. Technol.* **48**, 4298–4306 (2014).
10. World Health Organization. *Guidelines for Drinking-water Quality* 4th edn (World Health Organization, 2017).
11. Degueldre, C. A., Dawson, R. J. & Najdanovic-visak, V. Nuclear fuel cycle, with a liquid ore and fuel: toward renewable energy. *Sustain. Energ. Fuels* **3**, 1693–1700 (2019).
12. Rodríguez-Penalonga, L. & Soria, B. Y. M. A review of the nuclear fuel cycle strategies and the spent nuclear fuel management technologies. *Energies* **10**, 1235 (2017).
13. Yang, H. et al. Tuning local charge distribution in multicomponent covalent organic frameworks for dramatically enhanced photocatalytic uranium extraction. *Angew. Chem. Int. Ed.* **62**, e20230312 (2023).
14. Xie, Y. et al. Rational design of cooperative chelating sites on covalent organic frameworks for highly selective uranium extraction from seawater. *Cell Rep. Phys. Sci.* **4**, 101220 (2023).
15. Hao, M. et al. Converging cooperative functions into the nanospace of covalent organic frameworks for efficient uranium extraction from seawater. *CCS Chem.* **4**, 2294–2307 (2022).
16. Wu, Y. et al. Functional nanomaterials for selective uranium recovery from seawater: material design, extraction properties and mechanisms. *Coord. Chem. Rev.* **483**, 215097 (2023).
17. Yuan, Y. et al. Selective extraction of uranium from seawater with biofouling-resistant polymeric peptide. *Nat. Sustain.* **4**, 708–714 (2021).
18. Zhang, H. et al. Three mechanisms in one material: uranium capture by a polyoxometalate-organic framework through combined complexation, chemical reduction, and photocatalytic reduction. *Angew. Chem. Int. Ed.* **58**, 16110–16114 (2019).
19. Liu, T. et al. Removal and recovery of uranium from groundwater using direct electrochemical reduction method: performance and implications. *Environ. Sci. Technol.* **53**, 14612–14619 (2019).
20. Chen, Z. et al. Tuning excited state electronic structure and charge transport in covalent organic frameworks for enhanced photocatalytic performance. *Nat. Commun.* **14**, 1106 (2023).
21. Tsarev, S., Waite, T. D. & Collins, R. N. Uranium reduction by Fe(II) in the presence of montmorillonite and nontronite. *Environ. Sci. Technol.* **50**, 8223–8230 (2016).
22. O'Loughlin, E. J., Kelly, D. K., Cook, R. E., Csencsits, R. & Kemner, K. M. Reduction of uranium(VI) by mixed iron(II)/iron(III) hydroxide (green rust): formation of UO_2 nanoparticles. *Environ. Sci. Technol.* **37**, 721–727 (2003).
23. Pan, Z. Z. et al. Nanoscale mechanism of UO_2 formation through uranium reduction by magnetite. *Nat. Commun.* **11**, 4001 (2020).
24. Mollick, S. et al. Benchmark uranium extraction from seawater using an ionic macroporous metal–organic framework. *Energy Environ. Sci.* **15**, 3462–3469 (2022).
25. Liu, C. et al. A half-wave rectified alternating current electrochemical method for uranium extraction from seawater. *Nat. Energy* **2**, 17007 (2017).
26. Yuan, K. et al. Electrochemical and spectroscopic evidence on the one-electron reduction of U(VI) to U(V) on magnetite. *Environ. Sci. Technol.* **49**, 6206–6213 (2015).
27. Liu, X. et al. Highly efficient electrocatalytic uranium extraction from seawater over an amidoxime-functionalized In-N-C catalyst. *Adv. Sci.* **9**, e2201735 (2022).
28. Yang, H. et al. Functionalized iron-nitrogen-carbon electrocatalyst provides a reversible electron transfer platform for efficient uranium extraction from seawater. *Adv. Mater.* **33**, e2106621 (2021).
29. Chen, D. Y. et al. Self-standing porous aromatic framework electrodes for efficient electrochemical uranium extraction. *ACS Cent. Sci.* **9**, 2326–2332 (2023).
30. Wang, C. et al. Uranium in situ electrolytic deposition with a reusable functional graphene-foam electrode. *Adv. Mater.* **33**, e2102633 (2021).
31. Venna, S. R., Jasinski, J. B. & Carreon, M. A. Structural evolution of zeolitic imidazolate framework-8. *J. Am. Chem. Soc.* **132**, 18030–18033 (2010).
32. Liu, X. L. et al. Functional carbon capsules supporting ruthenium nanoclusters for efficient electrocatalytic $^{99}TcO_4^-/ReO_4^-$ removal from acidic and alkaline nuclear wastes. *Adv. Sci.* **10**, 2303536 (2023).
33. Kundu, S. et al. Electrocatalytic activity and stability of nitrogen-containing carbon nanotubes in the oxygen reduction reaction. *J. Phys. Chem. C.* **113**, 14302–14310 (2009).
34. Goulon, J., Friant, P. & Goulon-Ginet, C. Bridge-stacked polymeric structure of a fluorinated Ga(III) porphyrin deduced from a perturbed difference fourier analysis of EXAFS spectra. *Chem. Phys.* **83**, 367–375 (1984).
35. Zhang, Z. D., Zhu, J. X., Chen, S. H., Sun, W. M. & Wang, D. S. Liquid fluxional Ga single atom catalysts for efficient electrochemical CO_2 reduction. *Angew. Chem. Int. Ed.* **62**, e20221513 (2023).
36. Yang, H. et al. Emerging technologies for uranium extraction from seawater. *Sci. China Chem.* **65**, 2335–2337 (2022).
37. Mei, D., Liu, L. & Yan, B. Adsorption of uranium (VI) by metal-organic frameworks and covalent-organic frameworks from water. *Coord. Chem. Rev.* **475**, 214917 (2023).
38. Xie, Y. et al. Uranium extraction from seawater: material design, emerging technologies and marine engineering. *Chem. Soc. Rev.* **52**, 97–162 (2023).
39. Beltrami, D. et al. Recovery of uranium from wet phosphoric acid by solvent extraction processes. *Chem. Rev.* **114**, 12002–12023 (2014).
40. Feng, L. et al. In-situ synthesis of uranyl-imprinted nanocage for selective uranium recovery from seawater. *Angew. Chem. Int. Ed.* **61**, 82–86 (2021).
41. Rüdorff, W. & Valet, G. Über das ceruranblau und mischkristalle im system CeO_2-UO_2-U_3O_8. *Z. Anorg. Allg. Chem.* **271**, 257–272 (1953).
42. Lu, K. T., Zhang, Y. J., Aughterson, R. D. & Zheng, R. K. Uranyl oxide hydrate frameworks with lanthanide ions. *Dalton Trans.* **49**, 15854–15863 (2020).
43. Hund, F. & Peetz, U. Über weitere fluoritphasen in den mischoxyden seltener erden mit uran. untersuchungen der systeme La_2O_3, Nd_2O_3, Sm_2O_3, Yb_2O_3, Sc_2O_3 mit U_3O_8. *Z. Anorg. Allg. Chem.* **271**, 6–16 (1952).
44. Pointurier, F. & Marie, O. Use of micro-raman spectrometry coupled with scanning electron microscopy to determine the chemical form of uranium compounds in micrometer-size particles. *J. Raman Spectrosc.* **44**, 1753–1759 (2013).
45. Stefaniak, E. A. et al. Recognition of uranium oxides in soil particulate matter by means of μ-Raman spectrometry. *J. Nucl. Mater.* **381**, 278–283 (2008).
46. Petrov, V. A., Ojovan, M. I. & Yudintsev, S. V. Material aspect of sustainable nuclear waste management. *Sustainability* **15**, 11934 (2023).

47. Kreusch, J., Neumann, W., Appel, D. & Diehl, P. *Nuclear Fuel Cycle* (Heinrich Böll Foundation, 2006).
48. Rappe, A. K., Casewit, C. J., Colwell, K. S., Goddard Iii, I. W. A. & Skiff, W. M. UFF, A full periodic table force field for molecular mechanics and molecular dynamics simulations. *J. Am. Chem. Soc.* **114**, 10024–10035 (1992).

Acknowledgements

We acknowledge funding from the National Natural Science Foundation of China (Grants 22322603, U2167218, 22276054), the Beijing Outstanding Young Scientist Program. G.I.N.W. acknowledges a James Cook Research Fellowship from the Royal Society Te Apārangi. S.M. acknowledges the Robert A. Welch Foundation (B-0027). We also acknowledge support from the 14W station at the Shanghai Synchrotron Radiation Facility (SSRF).

Author contributions

H.Y., X.W. and S.M. conceived and designed the research. X.L., Y.X. and M.H. performed the synthesis and characterization and carried out the experiments. X.L., Y.L. and Z.C. performed and analyzed the TEM and DFT calculations. H.Y., X.W., G.I.N.W. and S.M. wrote the manuscript. All authors contributed to the discussion, and gave approval to the final version of the manuscript.

Competing interests

The authors declare no competing interests.

Additional information

Supplementary information The online version contains supplementary material available at https://doi.org/10.1038/s41467-024-52083-1.

Correspondence and requests for materials should be addressed to Hui Yang, Xiangke Wang or Shengqian Ma.

Peer review information *Nature Communications* thanks Fangting Chi, Shilpi Kushwaha, Ashish Maurya and the other, anonymous, reviewer for their contribution to the peer review of this work. A peer review file is available.